nature catalysis

Article

https://doi.org/10.1038/s41929-023-01010-6

Promoting Cu-catalysed CO_2 electroreduction to multicarbon products by tuning the activity of H_2O

Received: 11 July 2022

Accepted: 21 July 2023

Published online: 31 August 2023

Check for updates

Hao Zhang [1], Jiaxin Gao [1], David Raciti [2] & Anthony Shoji Hall [1]

The electrochemical reduction of CO_2 to valuable C_{2+} feedstocks is hindered by the competitive formation of C_1 products and H_2 evolution. Here we tuned the H_2O thermodynamic activity between 0.97 and 0.47 using water-in-salt electrolytes to obtain mechanistic insights into the role of H_2O in controlling C–C coupling versus C_1 product formation on Cu electrodes. By lowering the thermodynamic H_2O activity to 0.66, we obtained a Faradaic efficiency of ~73% at a partial current density of −110 mA cm^{-2} for C_{2+} products, at modest overpotentials. The adjustment of the thermodynamic H_2O activity provided fine control over C_{2+}/C_1 ratios, spanning a range from 1 to 20. The trends support the pivotal role of the thermodynamic H_2O activity in increasing the CO surface coverages and promoting C–C coupling to C_2 products. These findings highlight the potential of tuning thermodynamic H_2O activity as a guiding principle to maximize CO_2 reduction into highly desirable C_{2+} products.

The electrochemical reduction of CO_2 to chemical fuels is a promising strategy for lowering greenhouse gas emissions and, thus, mitigating catastrophic climate change. Presently, Cu and Cu alloys are the only materials capable of the electrochemical reduction of CO_2 to multicarbon products. However, these materials are not selective, often simultaneously forming CO, CH_4, $HCOO^-$, C_2H_4, ethanol (EtOH) and so on[1]. In general, there is a lack of rational guiding principles for designing reaction conditions that improve the selectivity of multicarbon products. Therefore, strategies that selectively reduce CO_2 to valuable multicarbon products (C_{2+}) for use as chemical feedstocks or energy-dense fuels must be developed.

The properties of the interface formed between a solid and an electrolyte (that is, the electric double layer) control the interfacial charge transfer, which influences the electrochemical behaviour of the system. Therefore, there are two primary methods for regulating the behaviour of an electrochemical system: alter the solid side of the interface or alter the solution side of the interface. Typical strategies for tuning the selectivity involve the development of new catalysts, the use of electrolyte additives, or altering the electrolyte composition[2–15]. Although methods for developing new catalysts are mature, rational strategies for modifying the solution side of the interface have not progressed to the same level of sophistication.

Several studies, dating back to the 1980s, have shown that alkaline pHs improve the selectivity toward C_2 products[1,10,16]. This is thought to occur because the rate-limiting step (RLS) of C_1 products involves proton transfer, whereas the RLS for the formation of C_2 products is thought to occur via C–C bond formation, which is a pH-independent process[17]. Weakly solvated cations such as Cs^+ or K^+ have been shown to improve the rate of CO_2 reduction to CO, $HCOO^-$, C_2H_4 and EtOH in comparison to strongly solvated cations such as Li^+ (refs. 2,3,18–21). The enhanced reduction of CO_2 to both C_1 and C_2 products on Cu electrodes due to cation-induced effects is predominately from an increase of the electric field intensity at the interface, which stabilizes key reaction intermediates[2,3,18–20,22]. Other reports have shown that highly concentrated electrolytes enhance CO_2 reduction, primarily due to hydroxide promotion or cation-induced electric field effects[23–26]. Recently, the modification of Cu interfaces with molecular additives such as *N*-alkylamines, amino acids and polymer films have emerged as viable methods for enhancing the formation of C_2 products[9,27]. It is hypothesized that changes to the double-layer structure resulting

[1]Department of Materials Science and Engineering, Johns Hopkins University, Baltimore, MD, USA. [2]Materials Science and Engineering Division, National Institute of Standards and Technology, Gaithersburg, MD, USA. e-mail: shoji@jhu.edu

from increased interfacial alkalinity, H bonding or specific adsorption of additives, improved the formation of C_2 products[23,28,29]. However, the molecular-level processes by which molecular additives or polymer overlayers control CO_2 reduction are poorly understood. One common observation among the approaches is that the polymer films or molecular additives contain hydrophobic moieties and, thus, control how H_2O is shuttled to the interface. Furthermore, highly concentrated alkali-metal hydroxides lower the activity of H_2O to as low as 0.6, but surprisingly, this has not been proposed as a mechanism for improving CO_2 reduction[30]. Therefore, we hypothesize that decreasing the supply of H_2O within the double layer is critical. This has been overlooked by the community and may lead to an enhanced reduction of CO_2 to C_{2+} products.

H_2O is the most practical solvent for CO_2 reduction because it is inexpensive. The transport of H_2O to the interface controls the proton supply for reactions with pH > 7. Since the reduction of CO_2 to any product (except $C_2O_4^{2-}$) necessitates a proton transfer step, the supply of the proton donor (that is H_2O) to the interface has a substantial impact on reactivity and selectivity. For example, CH_4 production is thought to involve proton transfer in its RLS, as shown by its pH-dependent reaction rate (on a pH-independent reference scale). The RLS for C_2 products, such as C_2H_4, is thought to proceed via the coupling of two CO*, which has a pH-independent reaction rate[31]. Note that there is a growing body of research proposing that the rate-determining step for C_2 product formation does not involve C–C coupling. Rather, these studies postulate that the protonation of CO* to COH* is integral[32]. Despite these insights, the exact mechanism underpinning C_2 product formation remains a vibrant topic of ongoing debate[32,33]. While pH-dependent experiments have yielded interesting fundamental insights, H_2O is present under all aqueous reaction conditions. Hence, there is always a viable proton donor present to mediate the reaction. Therefore, the fundamental processes by which H_2O, the principal proton donor in CO_2 reduction, impacts the branching between the C_1 and C_{2+} pathways need to be properly understood.

Recently, water-in-salt electrolytes were developed to enable aqueous alkali-metal-ion batteries[34]. The high salt concentrations in water-in-salt electrolytes disrupts the hydrogen bonding of H_2O and decreases the H_2O activity[34]. Furthermore, recent studies have shown that highly concentrated electrolytes exhibit an unusual interfacial H_2O structure[35,36]. Therefore, highly concentrated electrolytes can be used to uncover the role of H_2O in controlling the branching between C_1 and C_{2+} pathways without the use of an organic cosolvent.

Herein, we examine the role of H_2O in CO_2 reduction on Cu electrodes by utilizing highly concentrated $NaClO_4$ electrolytes. We demonstrated that the C_{2+}/C_1 ratios were enhanced by up to 20 when the thermodynamic H_2O activity (a_w) was lowered from 0.97 to 0.47, demonstrating the high tunability between C_1 and C_{2+} products. An optimized a_w of 0.66 enabled commercial Cu nanoparticles to achieve a total current density of ~170 mA cm^{-2} at −0.88 V versus the reversible hydrogen electrode (RHE) with a Faradaic efficiency (FE) of ~73% for C_2 and C_3 products (C_2H_4, EtOH and propanol (PrOH)). Furthermore, a kinetic analysis revealed that C_2 products exhibited negative reaction orders across a wide range of a_w, thus demonstrating that the restricted H_2O supply enhanced their formation at the expense of C_1 products. This study revealed that tuning the H_2O supply to electrified metal–solution interfaces is a robust method for promoting the formation of C_{2+} products.

Results

Structure of highly concentrated $NaClO_4$ solutions

High concentrations of $NaClO_4$ alter the chemistry of H_2O, causing changes to the structure of the bulk solution. To shed light on this effect, we interrogated the bulk solvent structure with Raman spectroscopy (Supplementary Fig. 1). The OH-stretching vibration of H_2O had a broad band between 2,700 and 4,000 cm^{-1} (Fig. 1a)[11,37].

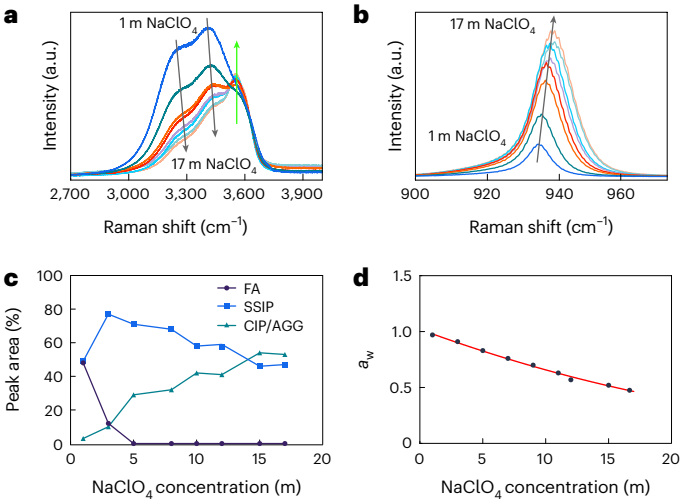

Fig. 1 | Physical properties of electrolytes as a function of NaClO4 concentration. **a**, OH-stretching vibration of water. **b**, ClO_4^- symmetric stretching vibration. **c**, Speciation of CIPs/AGGs (green triangles), FAs (purple circles) and SSIPs (blue squares) derived from **b**. The solid lines are guides for the eye. **d**, a_w as a function of $NaClO_4$ concentration derived from ref. 39. The red line represents the third-order fit of the data. The arrows in **a** and **b** point in the direction of increasing electrolyte concentration. The grey arrows and green arrow in **a** indicate vibrations associated with H-bonded water and ion-solvated water (that is isolated water), respectively.

The bands associated with the symmetric (~3,243 cm^{-1}) and asymmetric (~3,413 cm^{-1}) vibrational modes, which are sensitive to the hydrogen bonding of H_2O, decreased monotonically[37]. A high-frequency band around 3,570 cm^{-1} grew as the electrolyte concentration increased. This band was from H_2O coordinated to Na^+ and ion pairs. A broad band centred at ~938 cm^{-1}, which was from the symmetric stretching mode of ClO_4^-, was also observed (Fig. 1b)[38]. As the electrolyte concentration was increased, this band shifted to a higher frequency, indicating that the speciation of the ClO_4^- was altered. This band was deconvolved into three sub-bands: a low-frequency band at ~928 cm^{-1} from free anions (FAs), 937 cm^{-1} from solvent-separated ion pairs (SSIPs) and a band at ~943 cm^{-1} from contact ion pairs (CIPs) or aggregated ion pairs (AGGs) (Fig. 1c and Supplementary Fig. 2)[38]. Taken together, these data show that higher electrolyte concentrations disrupted hydrogen bonding and that a large portion of H_2O molecules were coordinated to Na^+ and ion pairs. The combination of these effects, along with lower H_2O concentration, resulted in a lower activity of H_2O with increasing salt concentration. Thus, highly concentrated solutions of $NaClO_4$ lower the availability of H_2O, which participates as a proton donor in CO_2 electroreduction. As a result, $NaClO_4$ concentrations from 1 to 17 m (where m is a unit molality, namely moles of solute per kg of solvent) enabled us to access a_w ranging from 0.97 to 0.47, respectively (Fig. 1d and Supplementary Table 1)[39].

CO_2 reduction on model Cu electrodes

Electrochemical experiments were performed with $NaClO_4$ electrolytes with a_w ranging from 0.97 to 0.47. CO_2 reduction on Cu electrodes was carried out with a leakless Ag/AgCl reference electrode (eDAQ) (Supplementary Tables 2–4). The model Cu electrodes were prepared by evaporating 25 nm of Cu (~0.02 mg cm^{-2} loading) onto the microporous side of a gas diffusion electrode (GDE) to form a thin layer of nanoparticles (Fig. 2a and Supplementary Fig. 3a–d). The electrochemically active surface area of the Cu electrodes was determined by performing cyclic voltammetry in the non-Faradaic region to ascertain the double-layer capacitance (Supplementary Fig. 4 and Supplementary Table 5). This configuration was chosen since a thin catalyst layer minimized the

https://doi.org/10.1038/s41929-023-01010-6

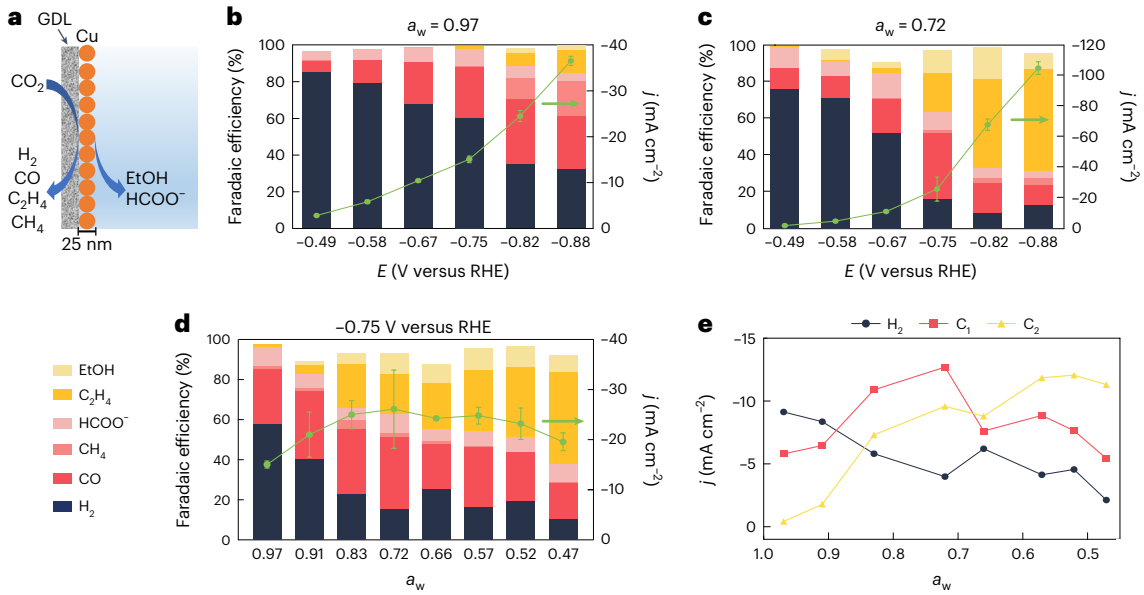

Fig. 2 | Electrochemical CO_2 reduction on a 25-nm-thick Cu-coated GDE. **a**, Schematic of the system. **b**,**c**, FE of EtOH, C_2H_4, CH_4, CO and $HCOO^-$; H_2 (bar graphs) and total current density (green circles) as a function of voltage for an a_w of 0.97 (**b**) and 0.72 (**c**). **d**, Dependence of the FE and total current density on the a_w of H_2; C_1 products and C_2 products collected at −0.75 V versus RHE. **e**, Partial current densities for H_2 (black circles), C_1 products (red squares) and C_2 products (yellow triangles). The error bars were removed for clarity and are presented in Supplementary Fig. 5. The error bars represent the s.d. derived from three repeated measurements, indicating the variability of the values. The solid lines are guides for the eye. GDL, gas diffusion layer.

mass transport resistance of ions and H_2O to the electrode surface. A GDE configuration was chosen to ensure the supply of CO_2 to the electrode was facile, allowing us to evaluate the system under kinetic control over a wide range of voltages. The evolved gases were sampled and quantified by in-line gas chromatography. Liquid products were quantified by nuclear magnetic resonance spectroscopy.

During CO_2 reduction on the 25 nm Cu-coated GDE, we observed a dependence on selectivity and current density with respect to a_w. For instance, when a fixed voltage of −0.82 V versus RHE was applied, we observed 10% FE for the production of C_2 products at $a_w = 0.97$. However, an increase in the FE for C_2 products was obesrved when a_w was lowered to 0.72, reaching a high of 66% (Fig. 2b,c). Interestingly, the dominant products at the high a_w of 0.97 were CO, CH_4 and H_2. Together, these products accounted for 92% to 81% of the FE, depending on the voltage. In contrast, at $a_w = 0.72$ and for voltages more negative than −0.82 V versus RHE, the dominant products observed were C_2H_4 and EtOH. Together, these products accounted for 66% of the FE. Interestingly, when a_w was lowered from 0.97 to 0.72, we observed a threefold increase in the current density (j) at −0.82 V and −0.88 V versus RHE. These results revealed that decreasing a_w improved the FE of C_2 products while simultaneously decreasing the FE of C_1 products and H_2.

To gain insight into the a_w-dependent CO_2 reduction, we assessed the FE and j of the reaction at −0.75 V versus RHE across different values of a_w (Fig. 2d,e). As a_w was lowered, we observed an increase in the FE of C_2 products from 1.4% to 42%, whereas the FE of C_1 products decreased from 46% to 28% (Fig. 2d). The j increased from ~14 to ~25 mA cm^{-2} as a_w was decreased to 0.83 then plateaued until a_w reached 0.52, before decreasing slightly. The best catalytic performance at −0.75 V versus RHE was observed at $a_w = 0.57$, yielding 31% C_2H_4, 11% EtOH, 30% CO, 1% CH_4 and 7% $HCOO^-$ with H_2 as the balance. To gain insights into the influence of a_w on the reaction kinetics, we examined the partial current density of the C_1 products, C_2 products and H_2 as a function of a_w (Fig. 2e and Supplementary Fig. 5). j_{C2} increased until a_w reached 0.57 and then plateaued, whereas j_{C1} increased until a_w reached 0.72, and then decreased for $a_w < 0.72$. j_{H2} consistently decreased as a_w was lowered. The promotion of CO_2 reduction to C_2 products was also observed at other voltages when a_w was reduced (Supplementary Fig. 6). Taken together, the data indicate that decreasing a_w enhanced the kinetics of C_2 product formation at the expense of H_2 and C_1 products, leading to improved C_2 product selectivity.

Reaction orders for CO_2 reduction on model Cu electrodes

To examine the role of H_2O on the branching between the C_1 and C_2 pathways, we determined the electrochemical reaction orders (ρ) of the products relative to a_w:

$$\rho = \left(\frac{\partial \log j_i}{\partial \log a_w}\right)_{E,P,T} \quad (1)$$

where j_i is the current density for the ith reaction, E is the potential, P is the pressure and T is the temperature. The reaction order for each irreversible reaction was measured versus a pH-independent reference scale, the normal hydrogen electrode (NHE)[40]. We chose −1.35 V versus NHE as the primary voltage for comparison.

Kinetic measurements at various a_w revealed that the C_2 and C_1 products had negative reaction orders of −5.8 and −2.6, respectively, for $a_w \geq 0.83$ at −1.35 V versus NHE (Fig. 3a). The large negative reaction order showed that the rate of C_2 products quickly rose as a_w was lowered. The slope for the reaction order of C_1 products was less negative than that of the C_2 products. A negative reaction order is indicative of an inhibitive effect, in which active sites become less available with increasing H_2O activity (that is, lower salt concentration)[41]. The hydrogen evolution reaction exhibited a positive reaction order of 1.7, indicating a systematic decrease of this reaction as a_w was lowered. This suggested that the surface coverage for Cu–H decreased with declining a_w since water decomposition was suppressed, thus making more active sites available for CO_2 electro-sorption. Furthermore, the range that we observed negative reaction orders for both the C_1 and C_2 products had an inverse trend with the population of the free anions in the bulk solution (Supplementary Fig. 7). This suggested that the electro-sorption of CO_2 could also be enhanced by a lower coverage of ClO_4^- anions on the electrode surface since it was trapped as ion pairs in the bulk solution

https://doi.org/10.1038/s41929-023-01010-6

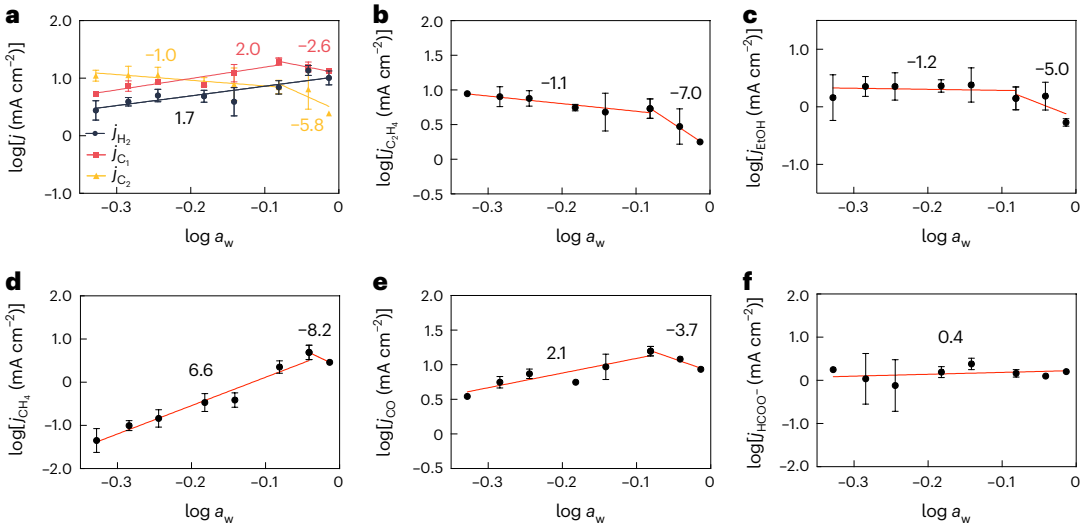

Fig. 3 | Reaction orders for CO_2 reduction as a function of a_w. **a**, Aggregate reaction order for C_1 products (red squares), C_2 products (yellow triangles) and H_2 (black circles). **b**–**f**, Reaction orders for C_2H_4 (**b**), EtOH (**c**), CH_4 (**d**), CO (**e**) and $HCOO^-$ (**f**). All data were collected at −1.35 V versus NHE on a 25-nm-thick evaporated Cu-coated GDE with $NaClO_4$ as the electrolyte. The error bars represent the s.d. derived from three repeated measurements, indicating the variability of the values. The red solid lines are linear fits of the data with numerical values of the reaction order.

or by changes to the potential dependence of water restructuring at the interface. Competitive adsorption between electrolyte anions, H_2O, Cu–H and adsorbed CO has been well documented in several reports in the literature, which support this idea[11,42,43]. Note that the CO_2 solubility in the bulk electrolyte decreased by 60% between 1 and 5 m $NaClO_4$, making it difficult to evaluate the competitive adsorption of these species under catalytic conditions via in situ infrared spectroscopy (Supplementary Fig. 8).

An increase in salt concentration may lead to enhancement of the cation-induced electric field, potentially contributing to an improved rate of CO_2 reduction to C_1 and C_2 products. However, the correlation between augmented salt concentrations and the density of cations on the electrode surface is not as direct as one might think. Recent studies have shown that the double-layer capacitance, which is an indicator of ion surface coverage, reaches saturation for concentrations exceeding 1 m, conforming to a Langmuir isotherm[44–46]. In our own examination employing electrochemical impedance spectroscopy, we noticed the capacitance reaching a saturation point for $NaClO_4$ concentrations near 0.5 m and then maintaining a nearly consistent level from 1 to 17 m (Supplementary Fig. 10e,f). This evidence implies that the surface coverage of cations may not markedly increase beyond 0.5 m due to saturation on the electrode surface. Thus, the probability of larger cation coverages on the electrode surface being the primary instigator for the improved catalytic enhancement for a_w below 0.83 is relatively low. Importantly, note that Fig. 3a–e have an inflection point at $a_w = 0.83$ (5 m $NaClO_4$ concentration), indicating a plausible role for cations in data above this threshold, whereas below it, cations appear less likely to have a significant influence on enhanced catalytic performance.

Reaction orders as a function of electrode thickness

To provide additional evidence that H_2O availability governs the reaction kinetics, we determined reaction orders relative to a_w at −1.30 V versus NHE for electrodes with different mass loadings (Fig. 4 and Supplementary Fig. 11). A thicker electrode will provide an additional impedance for H_2O transport, resulting in lower formation rates for products that involve proton transfer as part of the RLS.

We observed a rise in the C_1 reaction rate for the 25-nm-thick electrode for $a_w \geq 0.83$. However, we observed a decrease in the C_1 rate for $a_w \leq 0.83$ (Fig. 4a). The reaction order for C_1 products systematically shifted towards positive values with increasing electrode thickness, indicating that the formation of C_1 products became less favourable. Furthermore, the surface area-normalized rate of C_1 products decreased by approximately 20-fold as the electrode thickness was increased from 25 nm to 30 µm.

The C_2 products had a negative reaction order for a_w greater than approximately 0.7 to 0.8, regardless of the electrode thicknesses. For electrode thicknesses of 14 µm or greater, the reaction order transitioned to a weakly positive trend for $a_w \leq 0.72$ (Fig. 4b). This change in the trend can be attributed to the reduced availability of H_2O, which started to affect the reaction rate, potentially leading to a change in the mechanism. Interestingly, we observed a similar transition in reaction order from negative to positive for electrode thicknesses of 14 µm or greater, which is consistent with the change in reaction order observed for voltages ≤ −1.41 V versus NHE and $a_w \leq 0.72$ on electrodes with a thickness of 25 nm. (Supplementary Fig. 9). Interestingly, the surface area-normalized rate of the C_2 products was comparable across all electrode thicknesses, indicating that these products are less influenced by the availability of H_2O. These data demonstrate that the dominant driving force for the shift in reaction orders of C_2 products on 25-nm-thick model electrodes at higher overpotentials was H_2O transport.

Note that thicker electrodes can amplify the local hydroxide concentration. However, the current density of the electrodes reached a maximum for a_w between 0.83 and 0.72, indicating that the local hydroxide concentration peaked within this range (Supplementary Fig. 11). Despite the declining local hydroxide concentration for $a_w < 0.83$, the rate for C_1 products continued to decline substantially, whereas the rate for C_2 products was relatively stable (Fig. 4). This indicated that H_2O transport was the dominant factor that controlled the reaction selectivity rather than accumulation of OH^- at the interface. Collectively, the data indicate that C_2 products have a lower sensitivity to the availability of H_2O and can maintain high reaction rates across a wide range of electrode thicknesses. In contrast, the reaction rates of C_1 products decreased by approximately 20-fold, with reaction orders shifting towards larger positive values when even small perturbations occurred in the H_2O flux.

Potential-dependent CO adsorption for various H_2O activities

CO_2 reduction was evaluated by time-resolved electrochemical mass spectrometry (ECMS) to elucidate the adsorption dynamics of key reaction intermediates as a function of a_w and voltage. ECMS signals were

https://doi.org/10.1038/s41929-023-01010-6

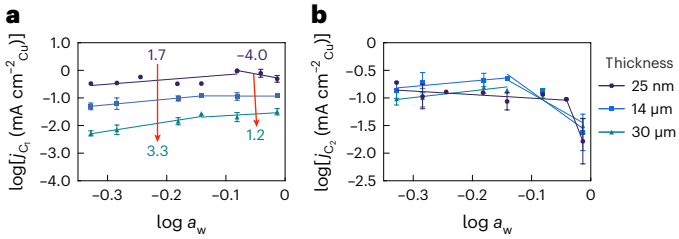

Fig. 4 | Porosity-dependent reaction orders as a function of a_w. a,**b**, C_1 (**a**) and C_2 (**b**) products collected at −1.30 V versus NHE with thicknesses of 25 nm (purple circles), 14 μm (blue squares) and 30 μm (green triangles). The current was normalized by the electrochemically active surface area of Cu (Supplementary Fig. 4 and Supplementary Table 5). The numbers in **a** are the numerical value of the reaction order. The error bars represent the s.d. derived from three repeated measurements, indicating the variability of the values. The solid lines on the graph represent linear fits of the data, providing numerical values for the reaction order.

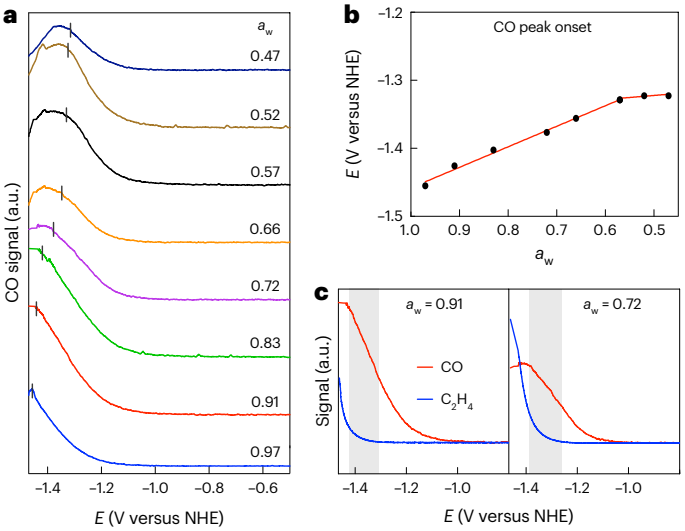

Fig. 5 | CO_2 reduction via time-resolved ECMS. a, CO signal (m/z = 28) as a function of potential via linear sweep voltammetry with a 1 mV s^{-1} scan rate in the cathodic direction on a 25-nm-thick Cu-coated GDE for various a_w. The grey vertical lines indicate the onset potential of the CO peak signal. **b**, Onset potential of the surface CO peak signal as a function of a_w. The red solid line is a guide for the eye. **c**, Overlays of the CO (red trace) and C_2H_4 (m/z = 27, blue trace) mass spectrometer signals. The left edge of the grey box is the onset potential of the CO surface peak, and its right edge is the onset potential for C_2H_4.

collected by sweeping the voltage from −0.5 to −1.47 V versus NHE at a 1 mV s^{-1} sweep rate while the GDE effluent gas was continuously sampled by a differentially pumped mass spectrometer. The ECMS data reveal the potential dependence of CO at different a_w (Fig. 5). The CO signal increased with the overpotential until it reached a peak, beyond which it declined. This maximum of the CO signal implies that CO coverage on the surface has peaked, as it represents an equilibrium state between the adsorbed CO and CO released from the surface. To gain further insights into the CO adsorption dynamics as influenced by a_w, we evaluated the lowest potential at which CO attained its highest coverage, termed the CO peak onset potential. This onset potential had a positive shift of approximately 150 mV on a pH independent reference scale when a_w was decreased from 0.97 to 0.66. No further noticeable change was observed for $a_w \leq 0.66$. This observation highlights that lower a_w values correspond to a decrease in the overpotential required for CO to reach peak coverage on the Cu surface. We postulate that an increased surface coverage of CO could amplify the interaction between CO adsorbates, thereby fostering improved C–C coupling. The signals for CO and C_2H_4 formation were overlaid to visualize the potential correlation between these species (Fig. 5c and Supplementary Fig. 12). Interestingly, the C_2H_4 onset potential occurs when the CO was approximately 50% of its peak value. This trend was found to hold across a wide range of a_w (Supplementary Fig. 13 and Supplementary Table 7). Therefore, we can conclude that high coverages of CO are necessary for C–C coupling to occur, and that lower a_w facilitates C–C coupling by increasing the surface coverage of CO.

Tafel slope analysis for CO_2 reduction on Cu model electrodes

Information about the reaction kinetics was obtained by analysing Tafel plots, which involve plotting log j versus E (NHE). The Tafel slope is given by:

$$\left(\frac{\partial \log E}{\partial \log j}\right)_{T,P} \tag{2}$$

This slope provides information about the number of electrons transferred between the resting state and the RLS of the catalytic cycle. Therefore, it is sensitive to changes in the reaction mechanism[40,47,48]. Changes to the mechanism from the modulation of a_w can be detected as variations in the Tafel slope.

The Tafel slopes were derived from constant-potential electrolysis with 25-nm-thick Cu-coated GDEs. The Tafel slopes for C_2H_4 were near 120 mV dec^{-1} at the lower potential range, then transitioned to approximately 70 mV dec^{-1} for a_w = 0.97 or 0.72 (Fig. 6a and Supplementary Table 8). A Tafel slope of 120 mV dec^{-1} implies that a one-electron transfer to form an adsorbed CO_2^- intermediate was the RLS for the formation of low C_2H_4 overpotentials[48]. For voltages <−1.2 V versus NHE, we observed a Tafel slope of approximately 70 mV dec^{-1}. This result indicates that the RLS was probably the reductive dimerization of CO intermediates to form a *OCCO dimer with fast kinetics (that is, with transfer coefficient $\alpha > 0.5$), since the steady-state coverage of adsorbed CO was high for a larger overpotential[49]. The adsorbed CO coverage was high for voltages <−1.2 V versus NHE, as confirmed by ECMS measurements, which indicates that the resting state of the catalyst was a CO-covered surface (Fig. 5c). For a_w = 0.47, the Tafel slopes for C_2H_4 formation changed to 82 mV dec^{-1} for voltages >−1.2 versus NHE, implying that electron transfer to form adsorbed *OCCO with fast kinetics was the RLS, since the electrode had high CO surface coverages, as confirmed by ECMS measurements (Supplementary Fig. 12). For more negative voltages (<−1.3 V versus NHE), the Tafel slope became infinite, suggesting that a chemical step that does not depend on electron transfer was rate-determining. This probably occurred because a very low a_w slowed down the proton transfer steps to the adsorbed *OCCO dimer, causing a mechanistic change in the reaction. To provide additional confirmation that proton transfer was not rate-limiting for C_2 product formation, we performed CO_2 reduction in D_2O as a solvent. We observed no kinetic isotope effect for the formation of C_2H_4, which agrees with the reaction order and Tafel slope data (Supplementary Fig. 14).

Tafel slopes of ~120 mV dec^{-1} were observed for all a_w in the formation of EtOH, suggesting that EtOH formation was rate-limited by electron transfer to CO to form an adsorbed *OCCO dimer for a system with high CO coverage at the resting state (Fig. 6b).

In contrast, the Tafel slopes for all C_1 products and H_2 were sensitive to changes of a_w. The Tafel slope for CH_4 increased from 60 mV dec^{-1} to 90 mV dec^{-1} and then finally to approximately 120 mV dec^{-1} as a_w decreased from 0.97 to 0.72 and then 0.47, respectively (Fig. 6c). A 60 mV dec^{-1} Tafel slope suggests the mechanism was rate-limited by a chemical step after a pre-equilibrium one-electron transfer, which is consistent with rate-limiting protonation of adsorbed CO to form a *CHO intermediate[40,48,50]. Positive reaction orders and Tafel slopes

https://doi.org/10.1038/s41929-023-01010-6

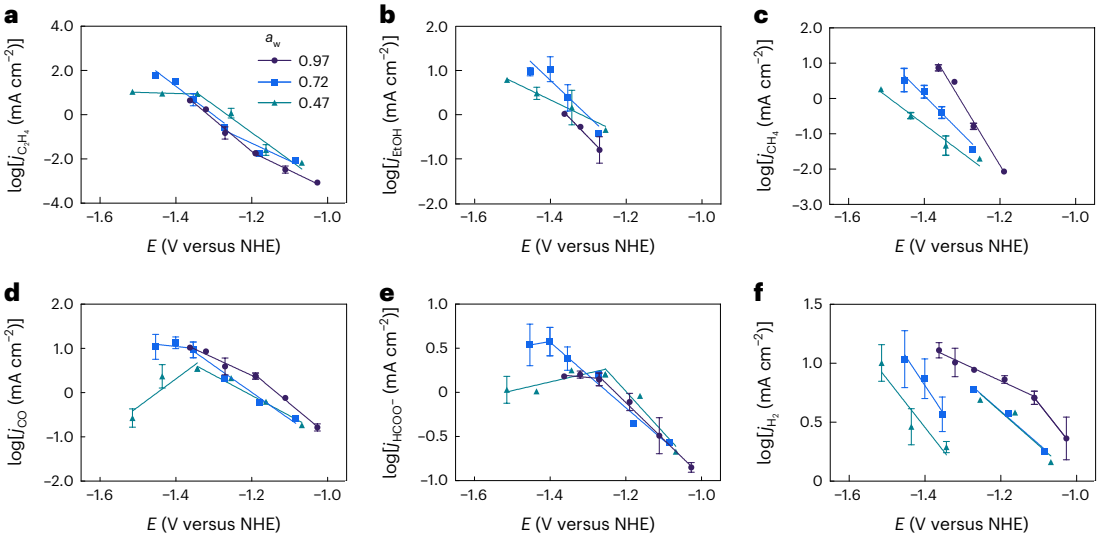

Fig. 6 | Tafel plots for CO_2 reduction products. a–f, C_2H_4 (**a**), EtOH (**b**), CH_4 (**c**), CO (**d**), $HCOO^-$ (**e**) and H_2 (**f**) at a_w of 0.97 (purple circles), 0.72 (blue squares) and 0.47 (green triangles). The data were collected with a 25-nm-thick Cu-coated GDE. The error bars represent the s.d. derived from three repeated measurements, indicating the variability of the values. The solid lines on the graphs represent linear fits of the data, providing numerical values for the Tafel slopes, as listed in Supplementary Table 8.

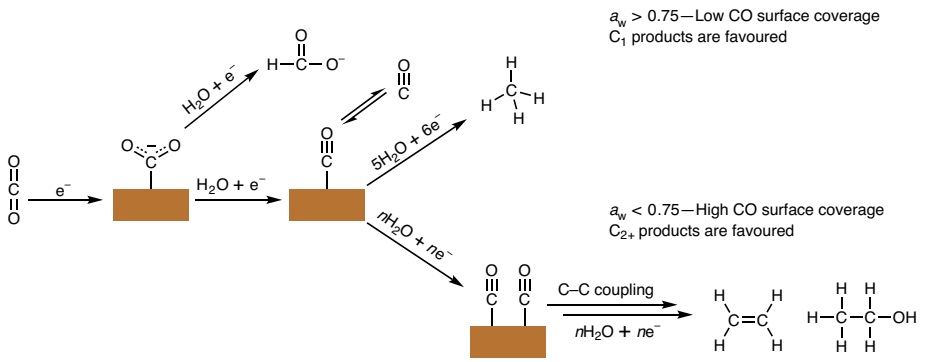

Fig. 7 | Simplified mechanisms for CO_2 reduction. Schematic depicting differences in the mechanism of CO_2 reduction on Cu electrodes for low and high a_w.

>90 mV dec^{-1} were observed for a_W < 0.72, suggesting that CH_4 production was rate-limited by the formation of adsorbed H* species when the H_2O availability was restricted.

CO had Tafel slopes of ~120 mV dec^{-1} and >250 mV dec^{-1} for $a_w \geq 0.72$ at low and high overpotential ranges, respectively (Fig. 6d). In the low overpotential range, a Tafel slope of near 120 mV dec^{-1} suggests that a one-electron transfer step was rate-limiting for CO formation. Tafel slopes of >250 mV dec^{-1} indicate that there is a weak potential dependence, suggesting that a chemical step was probably rate-limiting at high overpotentials. When a_w was lowered to 0.47, the Tafel slope was 210 mV dec^{-1} and −157 for the low and high overpotential ranges, respectively. Negative Tafel slopes imply that CO was consumed as the voltage was decreased. Reaction order data show that CO formation had a positive reaction order at all voltages for $a_w \leq 0.72$, which suggests that a proton transfer step may be rate-limiting (Fig. 3e). However, the CO coverage increased on the surface of the electrode as a_w was lowered, which suppressed CO evolution. Therefore, the reaction orders alone cannot determine whether CO was limited by a proton transfer step. We performed CO_2 reduction in D_2O and found no kinetic isotope effect. Therefore, a proton transfer step was not rate-limiting for CO formation (Supplementary Fig. 14). Taken together, the data indicate that CO production was rate-limited by the formation of adsorbed CO_2^- at low overpotentials. The observation of large Tafel slopes >200 (which implies weak potential dependence on rate) and then negative Tafel slopes indicate that CO was consumed as the voltage was swept more negatively to form C_{2+} products. This agrees with the ECMS results, which show that larger CO coverage is required for C–C coupling to occur (Supplementary Fig. 12).

$HCOO^-$ had Tafel slopes that were >200 mV dec^{-1} for all a_w in the low overpotential range, indicating that it has a weak potential dependence (Fig. 6e). At larger overpotentials, the Tafel slopes were infinite and then became negative with decreasing a_w. Taken together, the data indicate that the RLS for $HCOO^-$ is likely the protonation of CO_2^- at low overpotentials. At higher overpotentials, CO_2^- stays on the surface, which increases the surface coverages of CO.

H_2 exhibited similar Tafel slopes at all a_w for voltages <−1.3 V versus NHE (Fig. 6f). A break in the Tafel slope was observed at −1.3 V versus NHE for a_w = 0.72 or 0.47. This break coincided with a large increase in the generation of C_2 products and occurred at the potential where the Tafel slopes of CO and $HCOO^-$ became infinite. This suggests that the surface coverage of reaction intermediates, presumably adsorbed *CO, increased abruptly and displaced adsorbed Cu–H.

Based on the reaction orders relative to a_w, isotope experiments with deuterium and the Tafel slopes, we propose a simplified mechanistic scheme for CO_2 reduction on Cu (Fig. 7).

https://doi.org/10.1038/s41929-023-01010-6

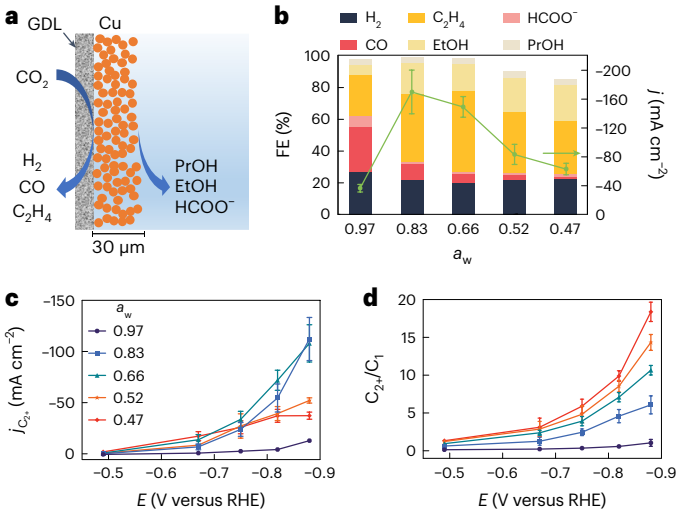

Fig. 8 | CO_2 reduction on Cu-nanoparticle-coated GDEs at various a_w. **a**, Schematic of the system. **b**, FE of PrOH, EtOH, C_2H_4, CO, $HCOO^-$ and H_2 as functions of a_w at −0.88 V versus RHE with an overlay of the total current density. **c**,**d**, Partial current density for C_{2+} products (**c**) and ratio of C_{2+}/C_1 as a function of voltage (**d**) at various a_w. The error bars represent the standard deviation derived from three repeated measurements, indicating the variability of the values. The solid lines serve as guides for the eye.

CO_2 reduction on high-surface-area Cu electrodes

We investigated whether a lower a_w can promote the reduction of CO_2 to multicarbon products on a GDE loaded with commercial copper nanoparticles (Fig. 8a). Cyclic voltammetry of the non-Faradaic region confirmed that the electrochemically active surface areas of all samples were comparable (Supplementary Table 5 and Supplementary Figs. 3 and 4). Constant-potential electrolysis at −0.82 V versus RHE revealed that the FE for C_{2+} products (C_2H_4, EtOH and PrOH) increased from 21% to 77%, whereas the FE for C_1 products (CO and $HCOO^-$) decreased monotonically from 36% to 11% as a_w was decreased from 0.97 to 0.66 (Fig. 8b). The FE then stabilized for lower a_w values. The C_{2+} products, which accounted for 77% of the total FE, were composed of 50% C_2H_4, 22% EtOH and 5% PrOH. Similar trends for the FE were observed at other voltages, indicating that C_{2+} products were enhanced while C_1 products were systematically suppressed by lower a_w (Supplementary Figs. 15 and 16). Interestingly, we observed PrOH as a product. The formation of CH_4 was completely suppressed on the porous electrodes, unlike the behaviour observed on model Cu electrodes.

To understand the origin of C_{2+} enhancement and the suppression of the C_1 products, we evaluated the partial current densities for the reaction. Remarkably, at −0.88 V versus RHE, j increased from 36 to approximately 170 mA cm^{-2} as a_w was decreased from 0.97 to 0.83 (Fig. 8b). It was stable at near 170 mA cm^{-2} until a_w = 0.66. However, upon a further decrease of a_w to below 0.66, j decreased to 63 mA cm^{-2}. Similar trends for the current density were observed for other voltages (Supplementary Fig. 15). The decreased current density at lower a_w was caused by mass transport limitations of H_2O, which likely induced a change in mechanism. We stress that protons are a necessary reactant for forming multicarbon products. However, protons do not affect the RLS, so environments with low proton donor availability can be tolerated to a certain extent.

The partial current densities revealed that the rate of C_{2+} product formation was enhanced by 10-fold and the C_1 product formation was decreased by 20-fold as a_w was decreased from 0.97 to 0.66 (Fig. 8c and Supplementary Fig. 16). The C_{2+}/C_1 ratios were enhanced by up to 20-fold by simply decreasing the activity of water (Fig. 8d). Remarkably, by optimizing a_w to 0.66, the system achieved a j_{C2+} of approximately 110 mA cm^{-2} with a FE of 73% at −0.88 V versus RHE on an unoptimized Cu catalyst.

Conclusions

By designing experimental conditions that enabled the activity of H_2O to be tuned in aqueous electrolytes, we were able to gain insights into how it controls the mechanism of electrochemical CO_2 reduction on Cu electrodes. Furthermore, optimized H_2O activities enabled us to reach a total current density of 170 mA cm^{-2} with 73% FE for C_{2+} products on unoptimized Cu catalysts with a high surface area. Our research found that the supply of H_2O dictates the bifurcation of CO_2 reduction from C_1 to C_{2+} products. Decreased H_2O activity led to an enhancement in the selectivity and current density of C_{2+} products (C_2H_4, EtOH and PrOH), while C_1 products and H_2 were simultaneously suppressed. This change in selectivity was caused by a shift in the onset potential of the peak CO formation to lower overpotentials. An analysis of kinetic data elucidated that the primary bottleneck in the generation of C_{2+} products occurs in the C–C coupling process, which depends on the coverage of CO on the electrode. This conclusion is supported by the observed correlation between CO coverage and C_2H_4 formation, a process that does not include rate-limiting proton transfer. Therefore, C_2 products had negative reaction orders for water activities from 0.97 to 0.47 at moderate overpotentials. In contrast, the dominant C_1 products, CO and CH_4, had a positive reaction order when the activity of H_2O was lowered below 0.83. This study demonstrates that decreasing the availability of the proton donor is a powerful method for enhancing the reduction of CO_2 to multicarbon products.

Methods

Materials

We used the following materials: sodium perchlorate hydrate ($NaClO_4 \cdot xH_2O$, 99.99% trace metals basis, Sigma-Aldrich, with the following heavy metals: barium <0.1 ppm (mg g^{-1}), calcium <0.1 ppm, magnesium 11.2 ppm, potassium 4.1 ppm, lithium 0.3 ppm and rubidium 0.2 ppm), CO_2 (research grade 99.999%, Airgas), deuterium chloride solution (35 wt% in D_2O, ≥99 at.% D, Sigma-Aldrich), deuterium oxide (D_2O, 99.9%, Cambridge Isotope Laboratories, Inc.), perchloric acid (70% $HClO_4$; Veritas Double Distilled, GFS Chemicals), copper pellets (Cu, 99.999% pure, Kurt J. Lesker), copper nanopowder (Cu, 25 nm particle size, Sigma-Aldrich), gas diffusion layer with a microporous layer (Freudenberg H15C13), isopropyl alcohol (American Chemical Society grade, Fisher Chemical), Nafion perfluorinated ion exchange resin solution (0.05 mass fraction in a mixture of lower aliphatic alcohols and water, Sigma-Aldrich), Nafion perfluorinated membrane (Nafion 117), leakless Ag/AgCl electrode (eDAQ) and platinum foil (Pt, 99.99% trace metals basis, Alfa Aesar).

Preparation of the electrode and the electrolyte

The 25 nm copper electrodes were prepared by thermal evaporation. Copper pellets were used as the metal source for deposition onto the microporous side of the gas diffusion layer. Deposition was performed at the rate of 1 to 2 Å s^{-1} at a base pressure of 10^{-6} torr (1.33×10^{-4} Pa) using a thermal evaporator (Torr International, Inc.).

Porous copper electrodes were made by applying ink over the GDE. The ink consisted of 9 mg of Cu powder, 1 ml of isopropyl alcohol and 2.7 μl of Nafion solution. It was prepared by mixing the components and sonicating for 30 min. To achieve a targeted metal loading, a specific volume of the ink mixture was placed into the holding chamber of an airbrush fitted with an air compressor (Master Airbrush). The ink was sprayed directly onto the microporous side of the gas diffusion layer (3 cm × 3 cm). Then, the sample was dried at 80 °C overnight. The mass loading was determined by weighing the carbon paper before and after the deposition of the ink. About 30% the Cu from the ink solution was lost during airbrushing.

A clean platinum foil was used as the counter electrode. The counter electrode compartment was separated from the working electrode compartment by a Nafion 117 membrane.

Various concentrations of $NaClO_4$ were used as the electrolyte. It was prepared with water purified from a Millipore system (resistance

>18.2 MΩ cm and <4 ppb (μg g^{-1})). Each concentration of the electrolyte was calculated based on molality (m, mol of solute per kg of solvent), which was the measured amount of solute per kg of water. The mixture was sonicated for 30 min at room temperature before each use. The molar concentration of water (M, moles of solute per litre of solution) was calculated based on the density at each concentration, using the weight of 1 ml of the solution. For the $NaClO_4 \cdot D_2O$ electrolyte, $NaClO_4$ was mixed with the D_2O and sonicated for 30 min then equilibrated at room temperature before each use.

pH and pD measurements of the electrolyte

Each electrolyte concentration was measured using a solid-state pH combination probe (pH Sensor InLab Expert Pro-ISM[51]) before catalysis. All measurements were conducted by acid titration[52–54]. For the pH and pD measurements, a small amount of concentrated $HClO_4$ or DCl, respectively, was added to the solution. The voltage of the solution was determined before and after the acid titration. The amount of acid added to the solution was determined gravimetrically. The following formula was used to determine the pH and pD of the solutions (Supplementary Table 4 and Supplementary Table 9):

$$E_{\text{test}} - E_{\text{ref}} = \frac{RT}{F}\ln|\gamma_{\text{test}} m_{\text{test}}| - \frac{RT}{F}\ln|\gamma_{\text{ref}} m_{\text{ref}}| = \frac{RT}{F}\ln\left|\frac{\gamma_{\text{test}} m_{\text{test}}}{\gamma_{\text{ref}} m_{\text{ref}}}\right| \quad (3)$$

where E_{test} is the potential reading from the pH meter before adding the acid, E_{ref} is the potential reading from the pH meter after adding the acid, R is the gas constant, T is room temperature, F is the Faraday constant, m_i is the proton concentration of the electrolyte in solution i and γ_i is the activity coefficient of solution i. The liquid junction potential was omitted since a solid-state reference probe was used. The junction potential must be accounted for if there are liquid–liquid junctions. The error bar was determined as the standard deviation of three repeated measurements. The amount of Na^+ in a solution was much higher than the amount of acid added to the solution. Therefore, it was assumed that $\gamma_{\text{test}} = \gamma_{\text{ref}}$. The pH of the solution can be estimated as $-\log m_{\text{ref}}$. All potential values in this work were calculated based on the pHs derived from the titration. A limitation of this method is the assumption of an activity coefficient of 1 for protons in highly concentrated electrolytes. Additionally, this method is not applicable for buffered solutions. To ensure the absence of buffering species, multiple titration points must be measured to observe a Nernstian change in potential.

Calibration of the reference electrode

The Ag/AgCl reference electrode was calibrated for each concentration of the $NaClO_4$ electrolyte, as shown in Supplementary Table 2. A clean electrochemical cell, glass bubbler and stir bar were used in each experiment. Each electrolyte was saturated with H_2 for 30 min. A Pt rotating-disc electrode was used as the working electrode, and a clean Pt mesh was used as the counter. The rotating-disc electrode was rotated at 1,600 rpm (1 rpm = 0.1047 rad s^{-1}) while the potential was swept at a rate of 10 mV s^{-1} versus the Ag/AgCl reference. The open circuit potential was taken to be 0 V versus RHE. All RHE and NHE values in this work were calculated based on the calibrated values of the reference to account for junction potentials and reference electrode drift.

Electrochemical impedance spectroscopy measurements

First, 1 cm^2 of copper foil was polished with a polishing pad. Then, it was dipped into concentrated HCl to remove the surface oxide. The foil was rinsed thoroughly with purified water (Millipore) and dried under N_2 before each measurement. The electrolyte was presaturated with CO_2 by sparging CO_2 directly into the bulk solution at a flow rate of 60 standard cubic centimetres per minute (sccm) for 30 min before the run. Impedance spectroscopy was performed at −1.21 V versus NHE to avoid discharging the capacitor due to high current densities at more negative potentials. The frequency ranged from 100 kHz to 1 Hz with a 10 mV amplitude (Metrohm Autolab with an electrochemical impedance spectroscopy module). The double-layer capacitance can be calculated from the electrochemical impedance spectroscopy data as follows[55]:

$$\text{DLC} = \left(R_2^{1-N} \times \text{CPE}\right)^{1/N} \quad (4)$$

where R_2 is the charge transfer resistance, CPE is the constant-phase element and N is a fitting parameter. Each element was fitted using the RelaxIS software (RHD Instruments) with the fitting circuit shown in Supplementary Fig. 9. A semicircle was observed in the Nyquist plot, indicating that the capacitance was coupled with the resistance. In this case, a constant-phase element was paired with a charge transfer resistance to describe this complex system. The behaviour of the capacitance was not ideal due to the inhomogeneity of the current density, the concentration gradients of the products or the surface roughness of the electrodes[56].

Electrochemical methods

Before electrolysis, cyclic voltammetry was conducted on each sample to prereduce the surface oxide. The potential was scanned from the open circuit potential to −1 V versus RHE with a scan rate of 100 mV s^{-1} for three cycles. An uncompensated resistance (R_u) was determined using electrochemical impedance spectroscopy (Supplementary Table 3), and 80% of R_u was applied at each potential. The final potential was iR corrected by the uncompensated resistance.

The electrode potentials were converted to the RHE scale using the following equation:

$$E_{\text{RHE}} = E_{\text{Ag/AgCl}} + 0.205 + 0.0591 \times \text{pH} + \phi_j \quad (5)$$

where ϕ_j is the junction potential, which was determined when calibrating the reference electrode, as described above.

The NHE potential was calculated using:

$$E_{\text{NHE}} = E_{\text{RHE}} - 0.0591 \times \text{pH} \quad (6)$$

The FE of a specific product was calculated using:

$$\text{FE\%} = \frac{ZnF}{Q} \times 100\% \quad (7)$$

where Z is the number of electrons exchanged to form a specific product from the reduction of CO_2, n is the number of moles of the product, F is the Faraday constant and Q is the total charge passed during electrocatalysis. All data points in this manuscript were collected by repeating each measurement on a fresh sample at least three times to calculate the standard deviation, which was used to establish error bars.

Detection of gas and liquid products

The gaseous reaction products were analysed with a gas chromatograph mass spectrometer (GCMS; Shimadzu GCMS-QP2020 SE). The instrument combines a single quadrupole mass spectrometer with a gas chromatograph (GC-2010 Plus). For gas separation, an Rt-Q-bond column (Restek, 30 m long with an inner diameter of 0.25 mm) was used. The GCMS was operated at 25 keV with the protection function turned off to allow for the detection of H_2 as $m/z = 2$. Gaseous products were collected every 10 min by directly venting the gas from the gas flow field of the working electrode of the GDE into the GCMS. The total flow into the gas chromatograph was 10 sccm (3 sccm into the GDE and 7 sccm to dilute the gas) at a back pressure of −0.260 psig (1 psi = 6,894.76 Pa). The liquid products were analysed by nuclear magnetic resonance spectroscopy (Bruker 400 MHz) using dimethyl sulphoxide (Sigma-Aldrich) as an internal standard and D_2O.

The one-dimensional ^{1}H spectrum was measured via water suppression by a presaturation method and all peak positions were shifted based on the standard peak of dimethyl sulphoxide (Supplementary Fig. 17).

Time-resolved ECMS measurements

ECMS was used to track the continuous evolution of gas products from the GDE during linear scan voltammetry (1 mV s^{-1}), which enabled the CO surface saturation potential to be determined. To perform these measurements, the outlet of the gas channel was connected to a custom-designed inlet connected to the electrochemical mass spectrometer (Spectroinlets) for real-time analysis of gas products in the effluent gas stream. To enable the evaluation of products that have a similar mass fragmentation as CO_2 (for example, CO), soft ionization parameters were implemented on the mass spectrometer using Spectroinlets Technical Notes 7 as a guide[57]. This mainly mitigated the influence of CO_2 in detecting CH_4 (15 AMU), C_2H_4 (27 AMU and 28 AMU) and CO (28 AMU). However, to fully assess the CO, the contribution of C_2H_4 to the 28 AMU had to be subtracted. To accomplish this, a stream of pure C_2H_4 was used to determine the ratio of 27 and 28 AMU. Then using the ratio and the 27 AMU trace, the contribution to 28 AMU was subtracted from the total 28 AMU detected. To determine the lag time between a product evolving at the GDE and its being detected by the mass spectrometer, potential pulses (50 to 100 µs) were applied to the cathode to produce a near instantaneous, finite amount of gas product that was then detected by the mass spectrometer. Supplementary Fig. 18 shows the lag time (6.3 s) for H_2 from a potential pulse to the peak of the signal from the mass spectrometer. H_2 was used as the primary way to analyse the lag time due to its facile kinetics.

The ECMS data were smoothed using the Savitzky–Golay smoothing function with 32 data points in a window with the OriginLab software. The onset potential of a species determined from ECMS measurements is defined as the potential where the signal-to-noise ratio >5 (ref. 58). The onset potential of the CO peak is defined as the potential at which it first starts to plateau, as determined by the first derivative using the OriginLab software.

Tafel slope and reaction order analysis

Tafel slopes represent the relationship between the overpotential and the logarithmic change of the current density. The Tafel slopes calculated for each product were determined from its partial current density. All data were collected using 25-nm-thick Cu-coated GDEs. The Tafel slopes were calculated with the following equation using data from constant-potential electrolysis collected every 10 min:

$$\text{Tafel slope} = \frac{\mathrm{d}E}{\mathrm{d}(\log j)} \tag{8}$$

where E is the applied overpotentials versus NHE, and j is the partial current density for the specific product.

Reaction orders were obtained using:

$$\text{Reaction order} = \frac{\mathrm{d}(\log j)}{\mathrm{d}(\log a_w)} \tag{9}$$

where j is the partial current density for the specific product and a_w is the thermodynamic water activity value for different electrolyte concentrations. a_w was extracted based on its value at room temperature[39].

Sample preparation for scanning electron microscopy

GDE samples (before and after catalysis) were cut into small pieces and taped onto the holder of the scanning electron microscope with double-sided carbon tape. A Thermo Scientific Helio G4 dual beam was used to collect scanning electron microscopy images (Supplementary Fig. 3).

Raman spectroscopy

A LabRam HR Evolution with a 633 nm He–Ne laser source in the backscattering configuration and a ×60 immersion lens objective was used to obtain Raman spectra of water and bulk $NaClO_4$ electrolytes at different concentrations. Each window of the spectrum was acquired using a grating with 1,800 lines per mm and a 2.54 cm charged coupled device detector (1,024 × 256 channels) with a 60 s acquisition time (Supplementary Fig. 1). The ionic aggregation of the ClO_4^- symmetric stretching mode for different water activities occurred around 920 to 970 cm^{-1}. Based on ref. 59, the peak can be deconvoluted into three regions (Supplementary Fig. 2a): free anions (at 933 cm^{-1}), solvent-separated ion pairs (at 935 cm^{-1}) and contact ion pairs/aggregated cation–anion pairs (at 942 cm^{-1}).

CO_2 solubility determination

A Fourier transform infrared spectrometer (Bruker Tensor II) with a HgCdTe (MCT) detector was used to collect infrared spectra of CO_2-saturated solutions as a function of $NaClO_4$ salt concentration. The spectrometer was operated at a scan rate of 30 kHz. Spectra were acquired with a spectral resolution of 4 cm^{-1}, and 32 interferograms were co-added for each spectrum. The aperture size was set to 4 mm. Pure water was used as the background. All spectra were shown in absorbance units defined as $-\log(I/I_0)$, where I and I_0 represent the sample and reference spectra. Before collecting each spectrum, CO_2 was purged into the solution for at least 1 h (80 sccm flow rate) to ensure the CO_2 was saturated[11,60]. The CO_2 asymmetric band area was used to determine its concentration (Supplementary Fig. 8a). The weight percentage of the dissolved CO_2 was calculated for each solution (Supplementary Fig. 8b) based on a method in ref. 60.

Kinetic isotope effect experiment

$NaClO_4$ solutions with concentrations of 3 m, 8 m, 12 m were made by mixing an appropriate amount of salt with H_2O or D_2O. The experiment was conducted using a 25-nm-thick Cu sample on a GDE at −1.42 V versus NHE. The run was repeated three times to establish the standard deviation for the error bars.

Data availability

All data are available in the figshare repository at https://doi.org/10.6084/m9.figshare.23692962 or from the corresponding author upon reasonable request.

References

1. Hori, Y., Murata, A., Takahashi, R. & Suzuki, S. Enhanced formation of ethylene and alcohols at ambient temperature and pressure in electrochemical reduction of carbon dioxide at a copper electrode. *J. Chem. Soc. Chem. Commun.* 17–19 (1988).
2. Murata, A. & Hori, Y. Product selectivity affected by cationic species in electrochemical reduction of CO_2 and CO at a Cu electrode. *Bull. Chem. Soc. Jpn* **64**, 123–127 (1991).
3. Resasco, J. et al. Promoter effects of alkali metal cations on the electrochemical reduction of carbon dioxide. *J. Am. Chem. Soc.* **139**, 11277–11287 (2017).
4. Hammer, B. & Nørskov, J. K. Theoretical surface science and catalysis—calculations and concepts. *Adv. Catal.* **45**, 71–129 (2000).
5. Watanabe, M., Shibata, M., Kato, A., Azuma, M. & Sakata, T. Design of alloy electrocatalysts for CO_2 reduction III. The selective and reversible reduction of CO_2 on Cu alloy electrodes. *J. Electrochem. Soc.* **138**, 3382–3389 (1991).
6. Kim, D. et al. Electrochemical activation of CO_2 through atomic ordering transformations of AuCu nanoparticles. *J. Am. Chem. Soc.* **139**, 8329–8336 (2017).
7. Zaza, L., Rossi, K. & Buonsanti, R. Well-defined copper-based nanocatalysts for selective electrochemical reduction of CO_2 to C_2 products. *ACS Energy Lett.* **7**, 1284–1291 (2022).

8. Wang, X. et al. Morphology and mechanism of highly selective Cu(II) oxide nanosheet catalysts for carbon dioxide electroreduction. *Nat. Commun.* **12**, 794 (2021).
9. Han, Z., Kortlever, R., Chen, H.-Y., Peters, J. C. & Agapie, T. CO_2 reduction selective for $C_{\geq 2}$ products on polycrystalline copper with N-substituted pyridinium additives. *ACS Cent. Sci.* **3**, 853–859 (2017).
10. Dinh, C. T. et al. CO_2 electroreduction to ethylene via hydroxide-mediated copper catalysis at an abrupt interface. *Science* **360**, 783–787 (2018).
11. Zhang, Z.-Q., Banerjee, S., Thoi, V. S. & Shoji Hall, A. Reorganization of interfacial water by an amphiphilic cationic surfactant promotes CO_2 reduction. *J. Phys. Chem. Lett.* **11**, 5457–5463 (2020).
12. Kuhl, K. P., Cave, E. R., Abram, D. N. & Jaramillo, T. F. New insights into the electrochemical reduction of carbon dioxide on metallic copper surfaces. *Energy Environ. Sci.* **5**, 7050–7059 (2012).
13. Li, C. W. & Kanan, M. W. CO_2 reduction at low overpotential on Cu electrodes resulting from the reduction of thick Cu_2O films. *J. Am. Chem. Soc.* **134**, 7231–7234 (2012).
14. Gomes, R. J. et al. Probing electrolyte influence on CO_2 reduction in aprotic solvents. *J. Phys. Chem. C* **126**, 13595–13606 (2022).
15. Dong, Q., Zhang, X., He, D., Lang, C. & Wang, D. Role of H_2O in CO_2 electrochemical reduction as studied in a water-in-salt system. *ACS Cent. Sci.* **5**, 1461–1467 (2019).
16. Whipple, D. T., Finke, E. C. & Kenis, P. J. A. Microfluidic reactor for the electrochemical reduction of carbon dioxide: the effect of pH. *Electrochem. Solid State Lett.* **13**, B109 (2010).
17. Gattrell, M., Gupta, N. & Co, A. A review of the aqueous electrochemical reduction of CO_2 to hydrocarbons at copper. *J. Electroanal. Chem.* **594**, 1–19 (2006).
18. Monteiro, M. C. O. et al. Absence of CO_2 electroreduction on copper, gold and silver electrodes without metal cations in solution. *Nat. Catal.* **4**, 654–662 (2021).
19. Malkani, A. S., Anibal, J. & Xu, B. Cation effect on interfacial CO_2 concentration in the electrochemical CO_2 reduction reaction. *ACS Catal.* **10**, 14871–14876 (2020).
20. Chan, K. A few basic concepts in electrochemical carbon dioxide reduction. *Nat. Commun.* **11**, 5954 (2020).
21. Thorson, M. R., Siil, K. I. & Kenis, P. J. A. Effect of cations on the electrochemical conversion of CO_2 to CO. *J. Electrochem. Soc.* **160**, F69–F74 (2012).
22. Ringe, S. et al. Understanding cation effects in electrochemical CO_2 reduction. *Energy Environ. Sci.* **12**, 3001–3014 (2019).
23. Luo, M. et al. Hydroxide promotes carbon dioxide electroreduction to ethanol on copper via tuning of adsorbed hydrogen. *Nat. Commun.* **10**, 5814 (2019).
24. Nesbitt, N. T. & Smith, W. A. Water and solute activities regulate CO_2 reduction in gas-diffusion electrodes. *J. Phys. Chem. C* **125**, 13085–13095 (2021).
25. Ren, W., Xu, A., Chan, K. & Hu, X. A cation concentration gradient approach to tune the selectivity and activity of CO_2 electroreduction. *Angew. Chem. Int. Ed.* **61**, e202214173 (5022).
26. Shin, S.-J. et al. A unifying mechanism for cation effect modulating C_1 and C_2 productions from CO_2 electroreduction. *Nat. Commun.* **13**, 5482 (2022).
27. Xie, M. S. et al. Amino acid-modified copper electrodes for the enhanced selective electroreduction of carbon dioxide towards hydrocarbons. *Energy Environ. Sci.* **9**, 1687–1695 (2016).
28. Li, J., Li, X., Gunathunge, C. M. & Waegele, M. M. Hydrogen bonding steers the product selectivity of electrocatalytic CO reduction. *Proc. Natl Acad. Sci. USA* **116**, 9220–9229 (2019).
29. Li, J. et al. Hydroxide is not a promoter of C_{2+} product formation in the electrochemical reduction of CO on copper. *Angew. Chem. Int. Ed.* **59**, 4464–4469 (2020).
30. Bro, P. & Kang, H. Y. The low-temperature activity of water in concentrated KOH solutions. *J. Electrochem. Soc.* **118**, 1430 (1971).
31. Nitopi, S. et al. Progress and perspectives of electrochemical CO_2 reduction on copper in aqueous electrolyte. *Chem. Rev.* **119**, 7610–7672 (2019).
32. Chang, X. et al. C–C coupling is unlikely to be the rate-determining step in the formation of C_{2+} products in the copper-catalyzed electrochemical reduction of CO. *Angew. Chem. Int. Ed.* **61**, e202111167 (2022).
33. Lu, X., Shinagawa, T. & Takanabe, K. Product distribution control guided by a microkinetic analysis for CO reduction at high-flux electrocatalysis using gas-diffusion Cu electrodes. *ACS Catal.* **13**, 1791–1803 (2023).
34. Suo, L. et al. Water-in-salt electrolyte enables high-voltage aqueous lithium-ion chemistries. *Science* **350**, 938–943 (2015).
35. Zhang, R. et al. Potential-dependent layering in the electrochemical double layer of water-in-salt electrolytes. *ACS Appl. Energy Mater.* **3**, 8086–8094 (2020).
36. Li, C.-Y. et al. Unconventional interfacial water structure of highly concentrated aqueous electrolytes at negative electrode polarizations. *Nat. Commun.* **13**, 5330 (2022).
37. Chen, Y., Zhang, Y.-H. & Zhao, L.-J. ATR-FTIR spectroscopic studies on aqueous $LiClO_4$, $NaClO_4$, and $Mg(ClO_4)_2$ solutions. *Phys. Chem. Chem. Phys.* **6**, 537–542 (2004).
38. Miller, A. G. & Macklin, J. W. Vibrational spectroscopic studies of sodium perchlorate contact-ion-pair formation in aqueous solution. *J. Phys. Chem.* **89**, 1193–1201 (1985).
39. Toner, J. D. & Catling, D. C. Water activities of $NaClO_4$, $Ca(ClO_4)_2$, and $Mg(ClO_4)_2$ brines from experimental heat capacities: water activity >0.6 below 200 K. *Geochim. Cosmochim. Acta* **181**, 164–174 (2016).
40. Gileadi, E. *Physical Electrochemistry: Fundamentals, Techniques and Applications* (Wiley-VCH, 2011).
41. Goyal, A. & Koper, M. T. M. The interrelated effect of cations and electrolyte pH on the hydrogen evolution reaction on gold electrodes in alkaline media. *Angew. Chem. Int. Ed.* **60**, 13452–13462 (2021).
42. Wuttig, A., Ryu, J. & Surendranath, Y. Electrolyte competition controls surface binding of CO intermediates to CO_2 reduction catalysts. *J. Phys. Chem. C* **125**, 17042–17050 (2021).
43. Ovalle, V. J. & Waegele, M. M. Impact of electrolyte anions on the adsorption of CO on Cu electrodes. *J. Phys. Chem. C* **124**, 14713–14721 (2020).
44. Aoki, K. J., He, R. & Chen, J. Double-layer capacitances caused by ion–solvent interaction in the form of Langmuir-typed concentration dependence. *Electrochem.* **2**, 631–642 (2021).
45. Xue, S., Garlyyev, B., Auer, A., Kunze-Liebhäuser, J. & Bandarenka, A. S. How the nature of the alkali metal cations influences the double-layer capacitance of Cu, Au, and Pt single-crystal electrodes. *J. Phys. Chem. C* **124**, 12442–12447 (2020).
46. Garlyyev, B., Xue, S., Watzele, S., Scieszka, D. & Bandarenka, A. S. Influence of the nature of the alkali metal cations on the electrical double-layer capacitance of model Pt(111) and Au(111) electrodes. *J. Phys. Chem. Lett.* **9**, 1927–1930 (2018).
47. Antipin, D. & Risch, M. Calculation of the Tafel slope and reaction order of the oxygen evolution reaction between pH 12 and pH 14 for the adsorbate mechanism. *Electrochem. Sci. Adv.* https://doi.org/10.1002/elsa.202100213 (2022).
48. Fletcher, S. Tafel slopes from first principles. *J. Solid State Electrochem.* **13**, 537–549 (2009).
49. Eberhardt, D., Santos, E. & Schmickler, W. Hydrogen evolution on silver single crystal electrodes—first results. *J. Electroanal. Chem.* **461**, 76–79 (1999).

50. He, M. et al. Selective enhancement of methane formation in electrochemical CO_2 reduction enabled by a Raman-inactive oxygen-containing species on Cu. *ACS Catal.* **12**, 6036–6046 (2022).
51. Thermo Scientific Orion ROSS pH Electrodes, User Manual. 263745-001, Rev. B, pg. 16. Nov. 2014.
52. Knauss, K. G., Wolery, T. J. & Jackson, K. J. A new approach to measuring pH in brines and other concentrated electrolytes. *Geochim. Cosmochim. Acta* **54**, 1519–1523 (1990).
53. Mesmer, R. E. Comments on A new approach to measuring pH in brines and other concentrated electrolytes by K. G. Knauss, T. J. Wolery, and K. J. Jackson. *Geochim. Cosmochim. Acta (USA)* **55** (1991).
54. Bard, A. J. & Faulkner, L. R. *Electrochemical Methods: Fundamentals and Applications*, 2nd edn. (Wiley, New York, 2001).
55. Singh, R. K., Devivaraprasad, R., Kar, T., Chakraborty, A. & Neergat, M. Electrochemical impedance spectroscopy of oxygen reduction reaction (ORR) in a rotating disk electrode configuration: effect of ionomer content and carbon-support. *J. Electrochem. Soc.* **162**, F489–F498 (2015).
56. Jorcin, J.-B., Orazem, M. E., Pebere, N. & Tribollet, B. CPE analysis by local impedance analysis. *Electrochim. Acta* **51**, 1473–1479 (2006).
57. SpectroInlets Soft Ionization EC-MS. Technical Note #7; https://spectroinlets.com/wpcontent/uploads/2022/01/Technical_note_7.pdf
58. Li, J. et al. Selective CO_2 electrolysis to CO using isolated antimony alloyed copper. *Nat. Commun.* **14**, 340 (2023).
59. Lee, M. H. et al. Toward a low-cost high-voltage sodium aqueous rechargeable battery. *Mater. Today* **29**, 26–36, 1369–7021 (2019).
60. Yu, H. & Obrovac, M. N. Quantitative determination of carbon dioxide content in organic electrolytes by infrared spectroscopy. *J. Electrochem. Soc.* **166**, A2467 (2019).

Acknowledgements

A.S.H. acknowledges financial support from the National Science Foundation under award no. CHE-2102648. H.Z. acknowledges the support from the National Science Foundation Graduate Research Fellowship under grant No. 2139757. Certain equipment, instruments, software or materials, commercial or non-commercial, are identified in this paper to specify the experimental procedure adequately. Such identification is not intended to imply recommendation or endorsement of any product or service by the National Institute of Standards and Technology, nor is it intended to imply that the materials or equipment identified are necessarily the best available for the purpose.

Author contributions

A.S.H. conceived the idea and supervised the project. H.Z. and J.G. designed and performed the electrolysis experiments and analysed the data. D.R. and H.Z. performed the differential ECMS experiments and the Raman spectroscopic analysis of the bulk solution. A.S.H., H.Z., D.R. and J.G. wrote the paper.

Competing interests

H.Z., J.G. and A.S.H. and their institutions have filed a US provisional patent application titled 'Controlling water activity to promote selective electrochemical reactions' (63/439,498). D.R. declares no competing interests.

Additional information

Supplementary information The online version contains supplementary material available at https://doi.org/10.1038/s41929-023-01010-6.

Correspondence and requests for materials should be addressed to Anthony Shoji Hall.

Peer review information *Nature Catalysis* thanks the anonymous reviewers for their contribution to the peer review of this work.